

# SHOCKS AND TIDES QUANTIFIED IN THE "SAUSAGE" CLUSTER, CIZA J2242.8+5301, USING N-BODY/HYDRODYNAMICAL SIMULATIONS

S. M. MOLNAR<sup>1</sup> AND T. BROADHURST<sup>2,3</sup>

*Draft version September 13, 2021*

## ABSTRACT

The colliding cluster, CIZA J2242.8+5301, displays a spectacular, almost 2 Mpc long shock front with a radio based Mach number  $M \simeq 5$ , that is puzzlingly large compared with the X-ray estimate of  $M \simeq 2.5$ . The extent to which the X-ray temperature jump is diluted by cooler unshocked gas projected through the cluster currently lacks quantification. Thus, here we apply our self-consistent N-body/hydrodynamical code (based on *FLASH*) to model this binary cluster encounter. We can account for the location of the shock front and also the elongated X-ray emission by tidal stretching of the gas and dark matter between the two cluster centers. The required total mass is  $8.9 \times 10^{14} M_{\odot}$  with a 1.3:1 mass ratio favoring the southern cluster component. The relative velocity we derive is  $\simeq 2500 \text{ km s}^{-1}$  initially between the two main cluster components, with an impact parameter of 120 kpc. This solution implies that the shock temperature jump derived from the low angular resolution X-ray satellite *Suzaku* is underestimated by a factor of two, due to cool gas in projection, bringing the observed X-ray and radio estimates into agreement. We propose that the complex southern relics in CIZA J2242.8+5301, have been broken up as the southerly moving "back" shocked gas impacts the gas still falling in along the collision axis. Finally, we use our model to generate Compton- $\gamma$  maps to estimate the reduction in radio flux caused by the thermal Sunyaev-Zel'dovich (SZ) effect. At 30 Ghz, this amounts to  $\Delta S_n = -0.072 \text{ mJy/arcmin}^2$  and  $\Delta S_s = -0.075 \text{ mJy/arcmin}^2$  at the locations of the northern and southern shock fronts respectively. Our model estimate agrees with previous empirical estimates that have inferred the measured radio spectra can be significantly affected by the SZ effect, with implications for charged particle acceleration models of the radio relics.

*Subject headings:* galaxies: clusters: general – galaxies: clusters: individual (CIZA J2242.8+5301) – methods: numerical

## 1. INTRODUCTION

Massive pairs of colliding clusters display extreme physical effects, including huge X-ray shock fronts that are often traced by radio "relics" of large-scale diffuse synchrotron emission (Enßlin 1999; for a recent review see Feretti *et al.* 2012). Cluster Collisions are often recognized by a clear bimodal distribution of member galaxies and dark matter mapped by weak and strong lensing effects. The shocked gas in the iconic "bullet cluster" (1E0657-56) clearly implies that two massive clusters have just passed centrally through each other with a high relative velocity of  $\gtrsim 3000 \text{ km s}^{-1}$  implied by the clearcut Mach cone found in its X-ray image (Markevitch *et al.* 2002). Velocities derived from X-ray observations using the shock jump conditions and N-body/hydrodynamical simulations support this interpretation (Mastropietro & Burkert 2008; Springel & Farrar 2007; Markevitch *et al.* 2004; Molnar *et al.* 2013a), with a wide range of model velocities derived, 2700–4500  $\text{ km s}^{-1}$  (for a recent review see Molnar 2015). The Bullet cluster provides model independent support for the simple, collisionless assumption regarding dark matter, because the bimodal weak lensing pattern is coincident galaxy distribution (Clowe *et al.* 2006), and hence, the dark matter must be essentially collisionless, like the member galaxies that have passed by each other during the first core passage.

The most massive cluster collisions have been uncovered in Sunyaev-Zel'dovich (SZ) sky surveys (ACT: Atacama Cosmology Telescope, Sifón *et al.* 2013; SPT: South Pole Telescope, Reichardt *et al.* 2012; Planck Satellite, Planck Collaboration *et al.* 2011), demonstrating that SZ selection favors cluster caught in collision when large columns of high pressure compressed gas are generated. A prime example is the strong SZ source, "El Gordo", that is a binary colliding cluster discovered by ACT (ACT-CL J0102-4915,  $z = 0.87$ ; Menanteau *et al.* 2012). Using N-body/hydrodynamical simulations, we have shown its cometary X-ray appearance can be readily reproduced by a collision that is not head on, generating two long, parallel tails of compressed gas, one of which has been pushed under gas pressure away from the most massive cluster component (Molnar & Broadhurst 2015) and the other tail is tidally compressed gas lying between the two cluster centers (see also the simulations by Zhang *et al.* 2015). This compressed gas in "El Gordo" lies interior to several relatively small radio "relics" that appear to mark shock boundaries at the interfaces of gas belonging to each cluster lying at large radius. It is difficult to detect merger socks because, although the pressure jump can be a factors of several, but the gas density is very low. However, a strong shock ( $M \gtrsim 3$ ) has been detected in "El Gordo" in the north-west around a radio relic (Botteon *et al.* 2016; Basu *et al.* 2016).

Much larger radio relics have been uncovered in other colliding clusters (e.g., 1RXS J0603.3+4214, the "Toothbrush" cluster, Ogrea *et al.* 2013b; CIZA J2242.8+5301, the "Sausage" cluster, Akamatsu *et al.* 2015; Ogrea *et al.* 2014; Ogrea *et al.* 2013a; van Weeren *et al.* 2010). In CIZA J2242.8+5301 a Mpc scale "sausage" shaped radio structure

<sup>1</sup> Institute of Astronomy and Astrophysics, Academia Sinica, P. O. Box 23-141, Taipei 10617, Taiwan

<sup>2</sup> Department of Theoretical Physics, University of the Basque Country, Bilbao 48080, Spain

<sup>3</sup> Ikerbasque, Basque Foundation for Science, Alameda Urquijo, 36-5 Plaza Bizkaia 48011, Bilbao, Spain

was found, which clearly corresponds to the gas collision shock front in the North, with its outer edge coincident with an X-ray temperature jump detected by Akamatsu et al. (2015). This shock front is the most clearly defined example known, spanning an angle of 80 deg. Its highly polarized radio emission implies the presence of a cluster scale magnetic field of  $\simeq 5 \mu\text{G}$  strength (van Weeren et al. 2010). The sausage also shows another large, but more diffuse radio relic in the south that lies close, but somewhat interior to the location of the southern X-ray shock claimed by Akamatsu et al. (2015). This X-ray shock front is expected to be generated in the “reverse” direction, opposite to the faster moving infalling cluster that has moved through to the north after the first core passage (Ricker & Sarazin 2001; Molnar et al. 2012; Molnar & Broadhurst 2015). No self-consistent hydrodynamical model has yet been constructed for CIZA J2242.8+5301 to date, and here we will also discuss this reverse shock front based on our simulations.

Several collision shocks have Mach number estimates from both radio and X-ray observations, e.g., A2255; 1RXS J0603.3+4214, the “Toothbrush” cluster; CIZA J2242.8+5301, the “Sausage” cluster (Akamatsu et al. 2016; Ogorean et al. 2013b; Akamatsu et al. 2015; Ogorean et al. 2014; Ogorean et al. 2013a; van Weeren et al. 2010), with a pattern emerging that the Radio estimates are generally significantly larger than the X-ray estimates. In principle, the X-ray estimates simply relate the physical temperature change across the shock to the standard Rankine-Hugoniot jump conditions. However, X-ray observations detect projected temperatures, which are derived from the observed spectrum as an integral through the entire cluster, so that temperature estimates at any projected radius can comprise gas with a spread of temperatures. Also, in practice, the X-ray emission is weak in the outer regions where the shocks are often seen (e.g., Akamatsu et al. 2015) requiring large area binning, and hence a large projected column of unshocked, cooler gas in each X-ray bin may flatten the temperature jump, biasing the Mach number low. This problem is exacerbated by the presence of very hot and luminous shocked gas, so that a model of the gas distribution in the LOS is beneficial to help estimate the effects of projection and derive the physical quantities of interest, including the density and temperature distribution of the gas. Such a model can be derived using full N-body/hydrodynamical simulations constrained by observations (e.g., Machado et al. 2015; Molnar & Broadhurst 2015).

Here we generate a comprehensive set of self-consistent N-body/hydrodynamical simulations of binary merging clusters of galaxies constrained by observations of member galaxies, gas, and dark matter to model CIZA J2242.8+5301, and thus obtain the 3-dimensional (3D) structure of the shocks (e.g., gas density, temperature distribution). We prefer to base the gas dynamics on the *FLASH* Adaptive Mesh refinement codes because of the presence of shocks that is not well captured by coarse grids or the “smooth particle hydrodynamics” approximation.

The structure of this paper is the following. In Section 2 we summarize results from previous analyses of CIZA J2242.8+5301 based on multifrequency observations and numerical simulations. We describe our simulation setup for modeling of CIZA J2242.8+5301 as a binary merger in Section 3. Section 4 presents our results, and provide a physical interpretation of the morphology of multifrequency observations of CIZA J2242.8+5301. In this section we also discuss quantitatively the merging shocks in CIZA J2242.8+5301, as

well as the biases in Mach numbers, derived from X-ray observations, and in flux measurements of radio relics due to SZ contamination from shocks. Section 5 contains our conclusions.

## 2. CIZA J2242.8+5301: A MERGING CLUSTER WITH THE PROTOTYPE OF RELICS

The most prominent radio relic is the northern relic in CIZA J2242.8+5301 (the “Sausage” Cluster: van Weeren et al. 2010). This is a bright radio relic, about 1.7 Mpc long, has a smooth bow or sausage shape (thus called the “sausage”), and it is only about 55 kpc wide, apparently delineating a merger shock. Assuming a diffusive shock acceleration (DSA) model (the most popular model to explain synchrotron radio emission from relics), van Weeren et al. (2010) derived a Mach number of 4.6. On the opposite side of this merging cluster, on the southern part, there are some scattered relics with irregular shape.

CIZA J2242.8+5301, at a redshift of  $z = 0.19$  (Jee et al. 2015), has been studied extensively. Detailed spectroscopic observations of CIZA J2242.8+5301 were carried out by Dawson et al. (2015). They found that the two subclusters have very similar redshifts, suggesting that the collision is close to the plane of the sky. *XMM-Newton* and *Chandra* observations of CIZA J2242.8+5301 were carried out to study the X-ray morphology and search for shocks and discontinuities in the X-ray emission by Ogorean et al. (2013a) and Ogorean et al. (2014).

Numerical simulations aiming to model the radio emission, and constrain the initial parameters of the merging clusters were carried out by van Weeren et al. (2011). They used N-body/hydrodynamical simulations (*FLASH*), but assumed fixed potentials for both subclusters. van Weeren et al. (2011) concluded that CIZA J2242.8+5301 is a binary merging cluster after the first core passage; the collision is close to the plane of the sky ( $\lesssim 10^\circ$  from the plane of the sky) with a mass ratio of  $\sim 2:1$  (the northern subcluster being more massive), and an impact parameter of  $\lesssim 400$  kpc. Weak lensing observations were used to derive the total mass of the system and the masses of the components of CIZA J2242.8+5301. Jee et al. (2015) found a total mass of  $M_{200c,total} \sim 2.1 \times 10^{15} M_\odot$ , a mass ratio  $\sim 1:1$ , and masses:  $M_{200c,1} = 11.0^{+3.7}_{-3.2} \times 10^{14} M_\odot$  and  $M_{200c,2} = 9.8^{+3.8}_{-2.5} \times 10^{14} M_\odot$  (200c refers to a density 200 times the critical mass density). Okabe et al. (2015) derived a total virial mass of  $M_{vir,total} \sim 1.9 \times 10^{15} M_\odot$  ( $M_{200c,total} \sim 1.6 \times 10^{15} M_\odot$ ), a mass ratio  $\sim 2:1$ , and masses:  $M_{vir,1} = 12.44^{+9.86}_{-6.58} \times 10^{14} M_\odot$  and  $M_{vir,2} = 6.74^{+7.64}_{-4.12} \times 10^{14} M_\odot$ , the southern subcluster found to be more massive. Northern and southern shocks were found around the relics with Mach numbers of  $2.7^{+0.7}_{-0.4}$  and  $1.7^{+0.4}_{-0.3}$  respectively, using *Suzaku* observations by Akamatsu et al. (2015).

Recently, the steepening of the spectra of the northern relic in CIZA J2242.8+5301, and the relic in 1RXS J0603.3+4214, the “Toothbrush” cluster, was found (Stroe et al. 2016), which excludes simple DSA models. Several solutions have been proposed to solve this problem using the northern relic in CIZA J2242.8+5301 as a prototype. Kang & Ryu (2016, 2015) proposed that fossil electrons (accelerated by the DSA mechanism) are reaccelerated as the shock runs them over; Fujita et al. (2016) suggested that cosmic rays are reaccelerated by turbulence generated behind shocks; Donnert et al. (2016) offered another explanation: magnetic turbulence generated by the amplification of the magnetic field is responsi-

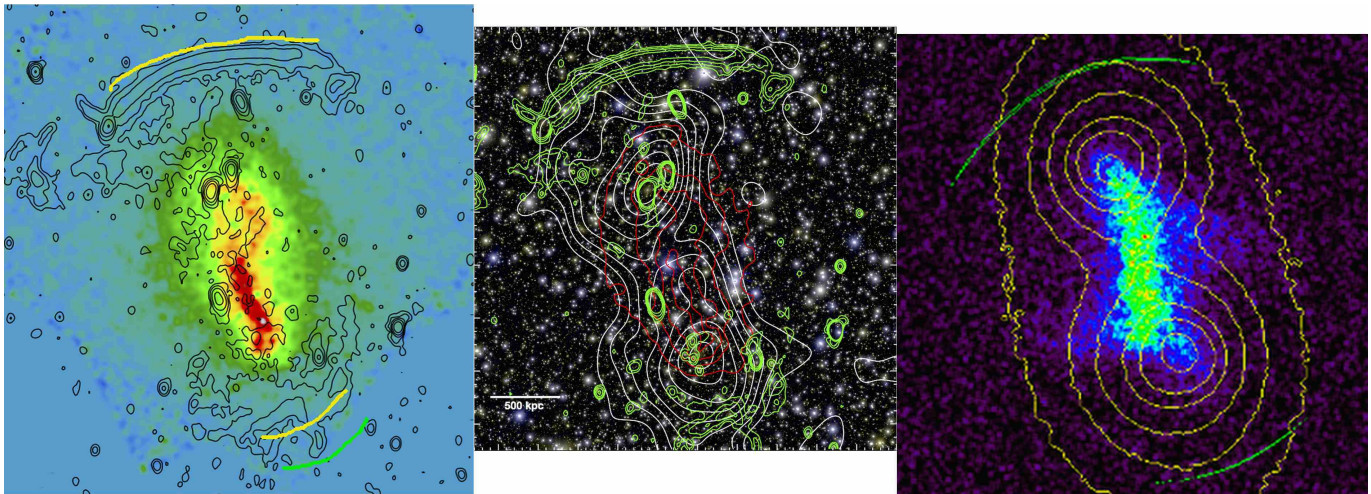


FIG. 1.— Images of CIZA J2242.8+5301 based on multi-wavelength observations and our best model derived using *FLASH* simulations. The first and second panels (from the left) show an image from *Chandra* observations (Figure 1 from Ogrea et al. 2014) overlaid the shock positions proposed by Akamatsu et al. (2015) (yellow lines; the light green line is our estimate for the position of the southern shock) and a Subaru image (gi color) with the galaxy number density contours (white contours), XMM-Newton X-ray luminosity (red contours), and Westerbork Synthesis Radio Telescope (WSRT) radio emission (green contours) overlaid (Figure 1 from Dawson et al. 2015). The third panel shows a simulated X-ray observation of our best model for CIZA J2242.8+5301 (run P120V25) with projected mass distribution overlaid (yellow contours). The northern and southern shocks are marked with green contours. The images are resized to the same physical scale (the length of the horizontal white bar in the middle panel is 500 kpc).

ble for the particle reacceleration. An alternative solution was suggested by Basu et al. (2016): the curved radio spectrum is a consequence of the SZ effect, which lowers the measured radio flux at the observed radio wavelengths ( $< 217$  GHz).

### 3. MODELING CIZA J2242.8+5301 USING HYDRODYNAMICAL SIMULATIONS

The main goal of our project was to obtain a reasonable physical model for CIZA J2242.8+5301 and study the merging shocks, not to carry out a systematic search for the initial parameters and determine their errors (that would require many more simulations).

#### 3.1. Details of the simulations, initial setup

We model CIZA J2242.8+5301 using 3D self-consistent N-body/hydrodynamic numerical simulations of binary galaxy cluster mergers including dark matter and intracluster gas. The simulations have been carried out using the publicly available parallel Eulerian adaptive mesh refinement (AMR) code *FLASH*, developed at the Center for Astrophysical Thermonuclear Flashes at the University of Chicago (Fryxell et al. 2000 and Ricker 2008).

We adopted a large box size, 13.3 Mpc on a side, for our simulations to capture the outgoing merger shocks. We used our well established method to initialize and run the merging cluster simulations (Molnar & Broadhurst 2015; Molnar et al. 2013a,b, 2012). We reach the highest resolution, 12.7 kpc at the centers of the clusters and at the merger shocks, as well as in the turbulent regions behind the shocks. Our simulations were semi-adiabatic: we included only shock heating, which is the most important non-adiabatic process for merging clusters.

We assumed spherical clusters with cutoffs at the the virial radius ( $r \leq R_{\text{vir}}$ ) for the the dark matter and the intracluster gas. Our initial conditions for the distribution of the dark matter was the NFW model (Navarro, Frenk & White 1997),

$$\rho_{\text{DM}}(r) = \frac{\rho_s}{x(1+x)^2}, \quad (1)$$

where  $x = r/r_s$ , and  $\rho_s, r_s = R_{\text{vir}}/c_{\text{vir}}$  are scaling parameters

for the radius and the density, and  $c_{\text{vir}}$  is the concentration parameter, and for the gas density distribution we adopted a non-isothermal  $\beta$  model,

$$\rho_{\text{gas}}(r) = \frac{\rho_0}{(1+y^2)^{3\beta/2}}, \quad (2)$$

where  $y = r/r_{\text{core}}$ , is the scaling parameters for the radius,  $\rho_0$ , is the density at the center, and  $r_{\text{core}}$  is the scaling parameter for the radius for the gas distribution.

We assumed hydrostatic equilibrium and derived the temperature from the equation of hydrostatic equilibrium adopting the ideal gas equation of state with  $\gamma = 5/3$ . We assumed  $\beta = 1$ , suggested by cosmological numerical simulations for the large scale distribution of the intracluster gas removing the filaments (Molnar et al. 2010). We used a gas fraction of 0.14, and represented the stellar matter in galaxies with collisionless particles, since galaxies can be considered collisionless for our purposes. The velocities of the dark matter particles were drawn from a Maxwellian distribution with a velocity dispersion as a function of distance from the cluster center obtained from the Jeans equation assuming isotropic velocity dispersion (Łokas & Mamon 2001). The distribution of the direction of the velocity vectors was assumed to be isotropic. More details of the set up for our simulations can be found in Molnar et al. (2012).

#### 3.2. FLASH Runs

We performed a series of *FLASH* simulations changing the masses, concentration parameters, impact parameter, and infall velocity of the system to find the best model for CIZA J2242.8+5301. Although the main goal of our study was not to carry out a systematic parameter search, in order to describe qualitatively the effect of changing initial parameters, we also show representative simulations which do not resemble CIZA J2242.8+5301. We list the initial parameters for those simulations we present in this paper in Table 1. The IDs of our runs are listed in the first column indicating the impact parameter ( $P$ ) in kpc and infall velocity ( $V$ ) in  $100 \text{ km s}^{-1}$  of each run as  $P_{ijkVlm}$ . The virial masses (in units of  $10^{14} M_{\odot}$ ) and



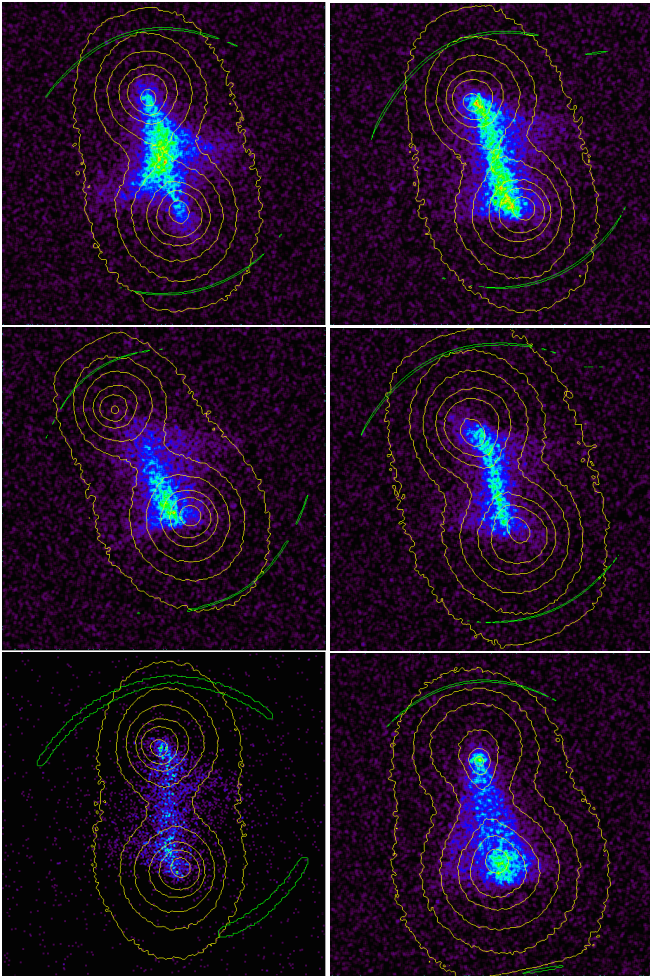


FIG. 2.— Models which do not match in detail CIZA J2242.8+5301. The color coding is the same as in the third panel in Figure 1. The two panels in the first row show simulations with the same initial parameters as our best model, but different impact parameters:  $P = 50$ , and  $180$  kpc (runs P050V25 and P180V25), the panels in the second and third row display images of runs with varying mass ratios, impact parameters and infall velocities (runs P100V25, P150V20, P150V30, and P200V18; see Table 1 for input parameters for our models).

concentration parameters of the two subclusters are shown in columns 2-5. In columns 6 and 7 we list the impact parameters in kpc and infall velocities in  $\text{km s}^{-1}$ .

#### 4. RESULTS AND DISCUSSION

##### 4.1. Deprojecting CIZA J2242.8+5301

We used the X-ray morphology, the positions of the merging shocks (Ogreaan et al. 2014; Akamatsu et al. 2015; van Weeren et al. 2010), and the positions of the dark matter centers of the two subclusters derived from weak lensing measurements of CIZA J2242.8+5301 (Okabe et al. 2015), to constrain the masses, the concentration parameters, the impact parameter, and the infall velocity of the system.

After each run, we rotated the system with an angle,  $\theta$ , out of the plane of the sky (assumed to coincide with the main plane of the collision containing the two cluster centers and the relative velocity vector) to match the projected distance with that of the observed (Okabe et al. 2015). The second rotation around the axis (“roll angle”) connecting the two dark matter centers with an angle,  $\varphi$ , was constrained by the observed X-ray morphology (Ogreaan et al. 2014). We choose

TABLE 1  
IDS AND INPUT PARAMETERS FOR DIFFERENT MODELS  
USED IN OUR HYDRODYNAMICAL SIMULATIONS.

ID <sup>a</sup>	$M_{\text{vir}1}$ <sup>b</sup>	$c_{\text{vir}1}$ <sup>b</sup>	$M_{\text{vir}2}$ <sup>c</sup>	$c_{\text{vir}2}$ <sup>c</sup>	$P$ <sup>d</sup>	$V_{\text{in}}$ <sup>e</sup>
P120V25	5.0	8	3.9	8	120	2500
P050V25	5.0	8	3.9	8	50	2500
P180V25	5.0	8	3.9	8	180	2500
P100V25	5.0	8	3.0	8	100	2500
P150V20	5.0	5	4.5	6	150	2000
P150V30	4.0	8	3.5	8	150	3000
P200V18	16.0	6	6.0	8	200	1800

<sup>a</sup> ID of the runs indicate the impact parameters in kpc and infalling velocities in  $100 \text{ km s}^{-1}$  and the mass of the main cluster in  $10^{14} M_{\odot}$ .

<sup>b</sup> Virial mass in  $10^{14} M_{\odot}$  and concentration parameter for the main cluster (1).

<sup>c</sup> Virial mass in  $10^{14} M_{\odot}$  and concentration parameter for the infalling cluster (2).

<sup>d</sup> Impact parameter,  $P$ , in units of kpc.

<sup>e</sup> Infall velocity of cluster 2,  $V_{\text{in}}$ , in  $\text{km s}^{-1}$ .

those outputs (epochs) which could be rotated in a way that the two merging shocks could be projected to match the observed positions (Akamatsu et al. 2015; Ogreaan et al. 2014). The shocks were located based on projected pressure gradients, a detailed description of our method to generate the X-ray and mass surface density maps can be found in Molnar & Broadhurst (2015).

We display images of CIZA J2242.8+5301 based on multi-wavelength observations and our best model in Figure 1. The first panel (from the left) shows an image from *Chandra* observations (Figure 1 from Ogreaan et al. 2014) overlaid the shock positions based on *Suzaku* observations proposed by Akamatsu et al. (2015) (yellow lines). Comparing the black and gray data points of the temperature around the southern relic on the left panel of Figure 7 of Akamatsu et al. (2015), we suggest that the southern shock is farther out than their estimate, it is located at the outer edge of the relics, shown as light green line in our figure (Figure 1). The second panel displays a Subaru image (gi color) with the galaxy number density contours (white contours), the XMM-Newton X-ray luminosity distribution (red contours), and the WSRT radio emission (green contours) overlaid (Figure 1 from Dawson et al. 2015). We show our best model for CIZA J2242.8+5301, which has a total virial mass of  $M_{\text{vir}} = 8.9 \times 10^{14} M_{\odot}$ , a mass ratio of 1.3:1, an impact parameter of  $P = 120$  kpc, and an infall velocity,  $V_{\text{in}} = 2500 \text{ km s}^{-1}$  (with rotations:  $\theta = 15^{\circ}$  and  $\varphi = 20^{\circ}$ ) in the third panel of Figure 1 (run P120V25). This model has a similar elongated – tidally stretched – X-ray morphology as CIZA J2242.8+5301, the positions of the dark matter peaks and the shocks also match the observations.

In Figure 2, we show models which do not fully resemble CIZA J2242.8+5301, but deviate significantly in one or more ways from the body of constraining data. The panels in the first row show models with the same initial parameters as our best model, but with an impact parameter that is either too small (50 kpc) or too large (180 kpc), resulting in a bulky X-ray core or a second peak in the north, respectively. In the second and the third row we show models, which have two large or too small mass ratios, or a very high infall velocity with a small mass ratio which produces the southern shock tilted more to the west than the observed one (1st panel in the third row). Our model with a more massive main cluster

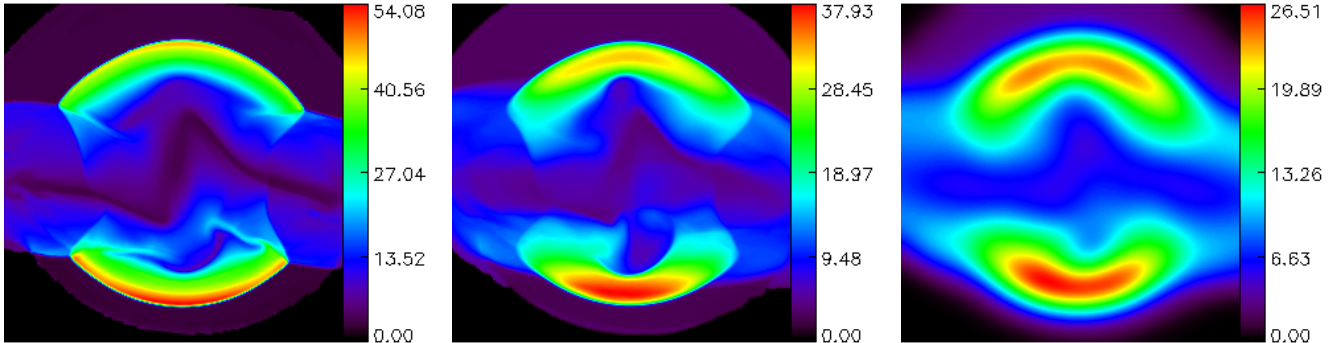


FIG. 3.— Temperature maps in units of keV from our best model for CIZA J2242.8+5301 (run P120V25). The high temperature regions (red/yellow) on the north and south mark the merging shocks moving outwards. Note that the collision axis is aligned vertically to match the shock geometry. *Left panel:* Physical temperature, 2D cut through the main plane of the collision. *Middle panel:* Spectroscopic temperature (Mazzotta et al. 2002). *Right panel:* Mock *Suzaku* observation.

(the total mass about the same as the one derived by Okabe et al. 2015, but with somewhat higher mass ratio, 2.66:1 vs. 2:1) show a thick X-ray bridge between the two dark matter centers not a thin, elongated feature as in CIZA J2242.8+5301 (2nd panel in the third row). For the input parameters of all models see Table 1. In general, very massive merging clusters ( $M_{\text{vir}} \sim 10^{15} M_{\odot}$ ) keep their gas and no thin tidal bridge would form between the two dark matter centers, and thus they do not look like CIZA J2242.8+5301.

#### 4.2. Properties of merging shocks in CIZA J2242.8+5301

Our simulations clearly demonstrate that the merging cluster, CIZA J2242.8+5301, is being seen just after the first core passage (in agreement with van Weeren et al. 2011) and before any subsequent core passages. The less massive infalling cluster, moving north, has passed the core of the main cluster and driving forward a bow shock currently located at the top of the images of the cluster (Figure 1). We predict a back shock propagating south, in the opposite direction to the infalling northern cluster. The two shocks are not expected to be symmetrical due to the different sizes of the merging clusters. Our simulations suggest that the northern subcluster is less massive in agreement with Okabe et al. (2015), and differing in conclusion with van Weeren et al. (2011), who suggest that the northern subcluster is more massive based on the argument that it has larger relics.

The pre-shock gas that lies ahead of the bow shock (the northern shock; to the right in Figure 4) is driven northwards by the gas pressure of the infalling cluster, but belongs to the main cluster. The pre-shocked gas behind the opposite shock (the southern shock) belongs to the infalling cluster and this back shock is moving faster relative to the pre-shock gas than the bow shock, and has a higher temperature. The position of this southern shock is depicted by the solid line in Figure 4).

The Mach number derived from the temperature jump at the shock in X-ray observations based on the Rankine-Hugoniot jump conditions is given by:

$$\frac{T_2}{T_1} = \frac{5\mathcal{M}^2 + 14\mathcal{M}^2 - 3}{16\mathcal{M}^2}, \quad (3)$$

where  $T_1$  and  $T_2$  are the pre- and post-shock temperatures, and  $\mathcal{M}$  is the Mach number (e.g., Botteon et al. 2016; Akamatsu et al. 2015; for a review see Markevitch & Vikhlinin 2007). Using the temperature jump from our simulations at the shocks in Equation 3, we obtain Mach numbers for the northern and southern shocks (the bow shock and back

shock):  $\mathcal{M}_{n,\text{simu}} = 6.5$  and  $\mathcal{M}_{s,\text{simu}} = 7.8$ . Based on our set of simulations, we find that, in general, the back shocks are stronger than the bow shocks in binary merging clusters having a larger temperature jump.

Our simulations predict spatially smooth shock fronts for the bow shock and the back shock (the northern and southern shocks as shown in Figure 1). For CIZA J2242.8+5301, the morphology of the radio emission associated with the bow shock is smooth, and very similar in curvature as our simulations predict. In the south the angular location of our predicted shock front is coincident with our predictions but always lies at a somewhat larger radius. Interestingly, the observed X-ray shock front is also claimed to lie at somewhat larger radius than the southern radio relics, although the precision of this position could be improved with deeper X-ray data. We also note that the observed radio structures that lie close the predicted back shock do not form a continuous sharp arc, but appears bifurcated with a more irregular morphology. A possible reason for this imperfect correspondence in the radio might be that the backward shock is impeded by subsequently infalling gas associated with the same filament that was connected to the infalling northern cluster. The next wave of shocks collides that has impeded and brakes up producing patchy relics that lag behind the predicted location of our ideal simulations.

#### 4.3. Bias in Mach numbers derived from X-ray observations

Some recent observations of merging clusters of galaxies show that the Mach numbers of merging shocks based on radio observations are about twice as large as those derived from X-ray observations (e.g., A2255:  $\mathcal{M}_{\text{radio}} = 2.7$ ,  $\mathcal{M}_{\text{xray}} = 1.4$ , Akamatsu et al. 2016; RX J0603.3+4214 (the ‘‘Toothbrush’’ cluster):  $\mathcal{M}_{\text{radio}} = 2.8$ ,  $\mathcal{M}_{\text{xray}} = 1.2$ , van Weeren et al. 2016; the northern shock in CIZA J2242.8+5301 (the ‘‘Sausage’’ cluster):  $\mathcal{M}_{\text{radio}} = 4.6$ ,  $\mathcal{M}_{\text{xray}} = 2.7$ , van Weeren et al. 2010; Akamatsu et al. 2015).

However, the physical gas temperature jump across the shock should be used in Equation 3, which is not observed. Only the projected temperature, which is the LOS integrated temperature weighted by the emission measure and convolved with the response function of the X-ray detector, can be derived from X-ray observations directly (i.e., without assuming a model for the LOS distribution of the gas). The usual method is to assume a simple geometry of the shock and use that model to deproject the observed image and derive the temperature jump (e.g., Menanteau et al. 2012). Some corrections are used occasionally to deal with the fall of the temper-

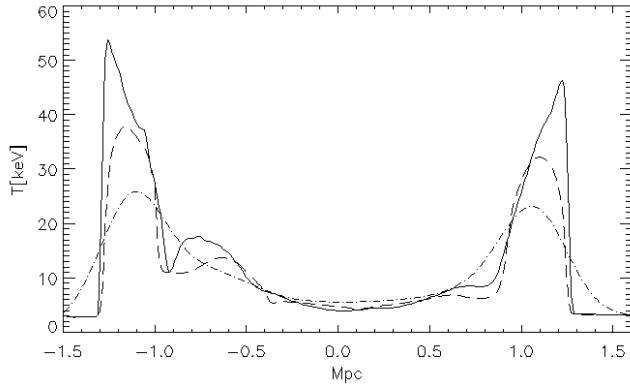


FIG. 4.— Temperature profiles across the bow shock (northern shock) and the back shock (southern shock) associated with the infalling and main cluster after the first core passage based on our best model (from Figure 3). Solid, dashed and dash-dotted lines represent the physical gas temperature, the spectroscopic temperature and a mock *Suzaku* observation.

ature with distance from the cluster center of the undisturbed (pre-shocked) cluster gas (e.g., Akamatsu et al. 2015).

In principle, the best way to deproject a merging cluster, and derive the Mach numbers for the shocks is to model the system using a full N-body/hydrodynamical code. We demonstrate the power of a full numerical simulation by comparing the Mach number we derived using the best model to that inferred from *Suzaku* observations of CIZA J2242.8+5301 (Akamatsu et al. 2015). The derivation of Mach numbers from *Suzaku* observations is difficult, because, in addition to the above mentioned problems with deprojection, it also has a low angular resolution of  $1'.6$ . Also, the shocked gas can reach a temperature of 20-50 keV, but the effective area of *Suzaku*'s X-ray Imaging Spectrometer (XIS) cuts off at about  $\sim 8$  keV and exponentially small for gas temperatures higher than 10 keV. Note, that this is also a problem for *Chandra* and *XMM-Newton*.

In Figure 3 we display temperature maps based on our best model for CIZA J2242.8+5301 (run P120V25). The left panel shows the physical temperature (2D cut through the main plane of the collision), the middle panel shows a temperature map taking into account projection effects (spectroscopic temperature of Mazzotta et al. 2002), and the right panel displays a mock *Suzaku* observation (spectroscopic temperature convolved with the point spread function, PSF of *Suzaku*). From this figure we can see that projection effects and a convolution with a low resolution PSF soften the shocks and they seem to be closer to the center of the merging clusters.

Figure 4 shows the temperature profile across the bow shock and the back shock associated with the infalling and main cluster after the first core passage. Solid, dashed and dash-dotted lines represent the physical gas temperature, the predicted spectroscopic temperature (Mazzotta et al. 2002), and a mock *Suzaku* observation based on the spectroscopic temperature (the spectroscopic temperature convolved with the PSF of *Suzaku*.) From this Figure, we can see that, due to projection effects and the low angular resolution, the measured temperature jump at the shocks by *Suzaku* would be biased low by a factor of two (compare the solid and dash-dotted temperature profiles). If  $T_2$  is underestimated by a factor of two, the Mach number,  $\mathcal{M}$ , derived from the temperature jump is going to be biased low by  $\Delta\mathcal{M} \sim 2$ .

Akamatsu et al. (2015), for example, measured a Mach number of  $\mathcal{M}_{n,A} = 2.7^{+7}_{-4}$  at the northern shock (bow shock) using *Suzaku* observations. Our N-body/hydrodynamical

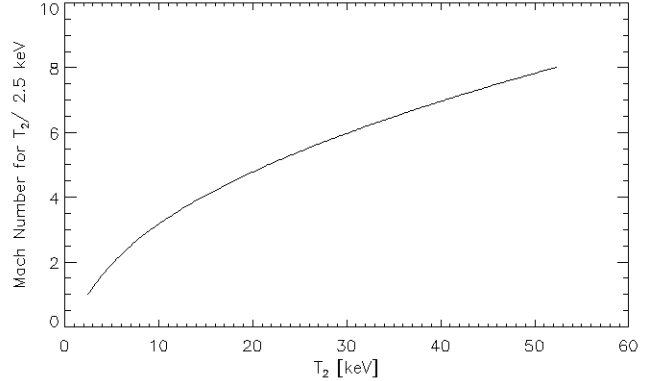


FIG. 5.— The Mach number as a function of post-shock temperature,  $T_2$ , holding the pre-shock temperature fixed at a value expected in the outer parts of a cluster,  $T_1 = 2.5$  keV. If  $T_2$  is underestimated by a factor of two, the derived Mach number,  $\mathcal{M}$ , is biased low by  $\Delta\mathcal{M} \sim 2$ .

simulations suggest a correction of about  $\Delta\mathcal{M} \sim +2$  for *Suzaku* observations. With this correction, the Mach number for the northern shock in CIZA J2242.8+5301 would be  $\mathcal{M}_{n,A,corrected} \sim 4.7$ . This corrected Mach number for the northern shock agrees well with  $\mathcal{M}_{n,radio} = 4.6^{+1.3}_{-0.9}$ , the value derived from radio observations by van Weeren et al. (2010).

However, averaging the projected temperature on a larger area in the sky further lowers the measured shock temperature, and thus the Mach numbers for the bow shock (northern) and the back shock (southern) derived by Akamatsu et al. (2015),  $\mathcal{M}_n = 2.7^{+0.7}_{-0.4}$  and  $\mathcal{M}_s = 1.7^{+0.4}_{-0.3}$ , are most likely biased even lower. Therefore, even with our suggested correction,  $\mathcal{M}_{n,A,corrected} \sim 4.7$ , we may underestimate the Mach number for the northern shock,  $\mathcal{M}_n$ . Note that using the temperature jump from our simulations, we obtain  $\mathcal{M}_{n,simu} = 6.5$  and  $\mathcal{M}_{s,simu} = 7.8$  (see Section 4.2).

We illustrate the bias in the Mach number due to measurement errors in the post-shock temperature in Figure 5. In this figure, using Equation 3, we show the Mach number as a function of post-shock temperature,  $T_2$ , holding the pre-shock temperature fixed at a value expected in the outer parts of a cluster,  $T_1 = 2.5$  keV. This figure suggests that, in general, if  $T_2$  is underestimated by a factor of two, the Mach number is going to be biased low by  $\Delta\mathcal{M} \sim 2$ .

#### 4.4. Bias in flux measurements of radio relics due to SZ contamination from shocks

Radio relics, found in the outskirts of clusters of galaxies, are elongated synchrotron radio sources with a length in the order of a Mpc. The radio emission of relics is highly polarized and have a steep spectrum. The relativistic electrons emitting the radiation are assumed to be accelerated to high energies by shocks in merging clusters (for a recent review see Feretti et al. 2012).

The main physical mechanism responsible for the particle acceleration at cluster merger shocks has not been identified yet. It is a subject of active research. The radio flux and the spectral index as a function of distance from the shock front provides important constraints on particle acceleration models, because they are related to ‘‘spectral aging’’ of the relativistic electrons due to synchrotron and inverse Compton energy losses. CIZA J2242.8+5301, the ‘‘Sausage’’ cluster, since in this cluster the projected distance from the shock gives a good approximation to the physical distance (the col-



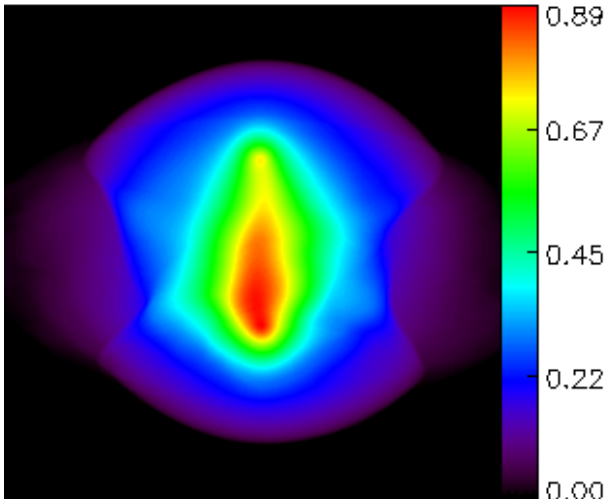


FIG. 6.— Compton- $y$  map of our best model for CIZA J2242.8+5301 (run P120V25). The figure is 3.1 Mpc a side. The units are Compton- $y \times 10^4$ . The infalling cluster passed the main cluster, it is moving north. The maximum of the Compton- $y$  parameter is around the core of the main cluster. Note that the collision axis is also aligned vertically, as in Figure 3.

lision is close to the plane of the sky), have been used to test different particle acceleration models, e.g., DSA mechanism (Stroe et al. 2016, also analyzed 1RXS J0603.3+4214, the “Toothbrush” cluster); fossil electrons (accelerated by the DSA mechanism) are reaccelerated as the shock runs them over (Kang & Ryu 2015); turbulent cosmic ray reacceleration (Fujita et al. 2016); and magnetic turbulence generated by the amplification of the magnetic field (Donnert et al. 2016).

DSA acceleration predicts a synchrotron power law spectrum. However, recent radio observations found curved spectra of some relics, which is inconsistent with the prediction of a simple DSA model (e.g., 1RX J0603.3+4214: van Weeren et al. 2016; CIZA J2242.8+5301: Stroe et al. 2016). Among other explanations (listed in the previous paragraph) it was suggested that around the shock front the thermal SZ effect may contaminate the radio flux measurements by lowering the measured flux from radio relics, and as a result, the radio spectrum becomes curved (e.g., Basu et al. 2016).

In Figure 6 we show the Compton- $y$  map of our best model for the merging cluster CIZA J2242.8+5301 (run P120V25). The units are Compton- $y \times 10^4$ . The infalling cluster passed the main cluster, it is located above it, and moving upward (north). The bow shock, ahead of the infalling cluster, moving north and the back shock moving south, can be clearly seen (sharp transition from dark blue to magenta). This predicted Compton- $y$  map can be used to test our model with future high resolution SZ observations.

In Figure 7 we show the Compton- $y$  profile, across the two shocks, extracted from the same data shown in Figure 6, as a function of distance from the cluster center (in Mpc). The infalling cluster passed the core of the main cluster, its center is located at about +0.6 Mpc, it is moving to the right. The center of the main cluster is at -0.5 Mpc. The sharp drop in the Compton- $y$  parameter associated with the bow shock (northern shock), ahead of the infalling cluster moving to the right, at +1.25 Mpc, and the back shock (southern shock) behind the main cluster moving to the left, at -1.3, can be clearly seen.

The Compton- $y$  parameter drops more than an order of magnitude at the merger shocks (see Figure 7). From the drop in the Compton- $y$  parameter, following Basu et al. (2016), we

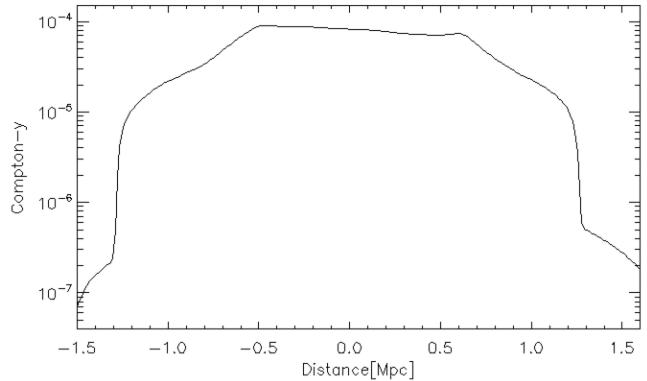


FIG. 7.— Compton- $y$  profile from Figure 6 across the two shocks as a function of distance from the cluster center (in Mpc). The infalling cluster, moving to the right, passed the core of the main cluster, its center is located at about +0.6 Mpc. The center of the main cluster is at -0.5 Mpc. The sharp drops in the Compton- $y$  parameter associated with the bow shock (northern shock) at +1.25 Mpc (ahead of the infalling cluster moving to the right) and the back shock (southern shock) at -1.3 (behind the main cluster moving in the left).

estimate the decrease in the radio flux density due to the SZ effect at the shocks using

$$\left( \frac{\Delta S_\nu}{\text{mJy/arcmin}^2} \right) = \frac{1}{340} \left( \frac{\Delta T_{\text{RJ}}}{\text{mK}} \right) \left( \frac{\nu}{\text{GHz}} \right)^2, \quad (4)$$

where  $\nu$  is the frequency in GHz,  $\Delta T_{\text{RJ}} = -2yT_{\text{CMB}}$  is the thermal SZ decrement in Rayleigh-Jeans radiation temperature in mK, and the drop of the radio flux is in  $\text{mJy/arcmin}^2$  (e.g., Birkinshaw 1999). We find that that at the northern and southern shocks at 30 GHz, the radio flux drops  $\Delta S_n = -0.072 \text{ mJy/arcmin}^2$  and  $\Delta S_s = -0.075 \text{ mJy/arcmin}^2$ .

## 5. CONCLUSIONS

We have performed a wide set of self-consistent N-body/hydrodynamical simulations (using *FLASH*) to seek a representative solution for CIZA J2242.8+5301, and to help understand better the level of deprojection on the Mach numbers of shocks affecting X-ray observations of this and other similar clusters. We have modeled CIZA J2242.8+5301 as a binary merger, constraining the initial parameters using lensing, X-ray and radio observations. The X-ray morphology and the locations of the two lensing centroids we find help constrain the impact parameter and the infall velocity. The positions of the outgoing shocks were constrained by X-ray and radio observations.

Our numerical simulations represent the first attempt to model CIZA J2242.8+5301 using self-consistent N-body/hydrodynamical simulations. We can appreciate from these simulations how tidal effects influence the gas distribution lying between the two clusters allowing us to identify suitable combinations of these initial parameters using the detailed X-ray morphology. Note that other models have not been able to benefit from this. For example, van Weeren et al. (2011) assumed, for simplicity, fixed non-interacting shapes for the gravitational potentials of the two merging clusters moving on pre-calculated paths.

We have demonstrated that low angular resolution X-ray telescopes (e.g., *Suzaku*) significantly underestimate the shock temperature as much as a factor of two, and thus the resulting Mach number may be biased low by  $\Delta \mathcal{M} \sim 2$ . Adding this correction to the *Suzaku* result for the Mach number of the northern shock,  $\mathcal{M}_{n,A} \sim 2.7$  (Akamatsu et al. 2015), we obtain

$\mathcal{M}_{n,A,corrected} \sim 4.7$ , which agrees well with the result from radio observations,  $\mathcal{M}_{n,radio} = 4.6$  (van Weeren et al. 2010).

We have suggested that the relics around the northern and southern shocks in CIZA J2242.8+5301 look different, the southern relics, in contrast to our simulations, are patchy and irregular in shape, perhaps because of a filament of gas that follows the infalling northern cluster has impeded and disturbed the back shock on its way out towards the south colliding with the subsequently infalling filament of gas.

The main mechanism for particle acceleration around shocks in merging galaxy clusters is an active subject of research. The shape of the radio spectrum from radio relics located around shocks provides constraints on particle acceleration models associated with shocks. However, the thermal SZ effect associated with the dense shocked gas may act to significantly lower the measured radio flux at shocks, as a function of frequency. We have simulated Compton- $\gamma$  maps based on our best model for CIZA J2242.8+5301, and shown that the drops in the Compton- $\gamma$  parameter due to the merging shocks may reach more than one order of magnitude. Our model in-

dicates that at the northern and southern shocks at 30 GHz, the radio flux drops  $-0.072$  mJy/arcmin<sup>2</sup> and  $-0.075$  mJy/arcmin<sup>2</sup>. This sharp discontinuity, however, is smoothed out by the PSF of the observing radio telescopes. In agreement with Basu et al. (2016), we find that merging shocks may considerably reduce the measured flux of radio relics depending mainly on the masses and relative velocities of the merging clusters.

We thank Huub Röttgering for discussions on the interpretation of the radio data. The code *FLASH* used in this work was in part developed by the DOE-supported ASC/Alliance Center for Astrophysical Thermonuclear Flashes at the University of Chicago. We thank the Theoretical Institute for Advanced Research in Astrophysics, Academia Sinica, for allowing us to use its high performance computer facility for our simulations. This research has made use of the NASA/IPAC Extragalactic Database (NED) which is operated by the Jet Propulsion Laboratory, California Institute of Technology, under contract with the National Aeronautics and Space Administration.

#### REFERENCES

- Akamatsu, H., Mizuno, M., Ota, N., et al. 2016, arXiv:1612.03058  
 Akamatsu, H., van Weeren, R. J., Ogrea, G. A., et al. 2015, *A&A*, 582, A87  
 Basu, K., Sommer, M., Erler, J., et al. 2016, *ApJ*, 829, L23  
 Basu, K., Vazza, F., Erler, J., & Sommer, M. 2016, *A&A*, 591, A142  
 Birkinshaw, M. 1999, *Phys. Rep.*, 310, 97  
 Botteon, A., Gastaldello, F., Brunetti, G., & Kale, R. 2016, *MNRAS*, 463, 1534  
 Clowe, D., Bradač, M., Gonzalez, A. H., et al., 2006, *ApJ*, 648, L109  
 Dawson, W. A., Jee, M. J., Stroe, A., et al. 2015, *ApJ*, 805, 143  
 Donnert, J. M. F., Stroe, A., Brunetti, G., Hoang, D., & Roettgering, H. 2016, *MNRAS*, 462, 2014  
 EnBlin, T. A. 1999, *Diffuse Thermal and Relativistic Plasma in Galaxy Clusters*, 275  
 Ferretti, L., Giovannini, G., Govoni, F., & Murgia, M., 2012, *A&A Rev.*, 20, 54  
 Fujita, Y., Akamatsu, H., & Kimura, S. S. 2016, *PASJ*, 68, 34  
 Fryxell, B., et al. 2000, *ApJS*, 131, 273  
 Jee, M. J., Stroe, A., Dawson, W., et al. 2015, *ApJ*, 802, 46  
 Kang, H., & Ryu, D. 2015, *ApJ*, 809, 186  
 Kang, H., & Ryu, D. 2016, *ApJ*, 823, 13  
 Łokas, E. L., & Mamon, G. A. 2001, *MNRAS*, 321, 155  
 Machado, R. E. G., Monteiro-Oliveira, R., Lima Neto, G. B., & Cypriano, E. S. 2015, *MNRAS*, 451, 3309  
 Markevitch, M., Gonzalez, A. H., David, L., et al. 2002, *ApJ*, 567, L27  
 Markevitch, M., & Vikhlinin, A., 2007, *Phys. Rep.*, 443, 1  
 Markevitch, M., Gonzalez, A. H., Clowe, D., et al. 2004, *ApJ*, 606, 819  
 Mastroiello, C., & Burkert, A. 2008, *MNRAS*, 389, 967  
 Mazzotta P., Rasia E., Moscardini L., & Tormen G., 2004, *MNRAS*, 354, 10  
 Menanteau, F., Hughes, J. P., Sifón, C., et al., 2012, *ApJ*, 748, 7  
 Molnar, S. 2015, *Frontiers in Astronomy and Space Sciences*, 2, 7  
 Molnar, S. M., & Broadhurst, T. 2015, *ApJ*, 800, 37  
 Molnar, S. M., Broadhurst, T., Umetsu, K., et al. 2013, *ApJ*, 774, 70  
 Molnar, S. M., Chiu, I.-N. T., Broadhurst, T., & Stadel, J. G. 2013, *ApJ*, 779, 63  
 Molnar, S. M., Hearn, N. C., & Stadel, J. G. 2012, *ApJ*, 748, 45  
 Molnar, S. M., et al. 2010, *ApJ*, 723, 1272  
 Navarro, J. F., Frenk, C. S., & White, S. D. M. 1997, *ApJ*, 490, 493  
 Ogrea, G. A., Brüggén, M., van Weeren, R., et al. 2014, *MNRAS*, 440, 3416  
 Ogrea, G. A., Brüggén, M., Röttgering, H., et al. 2013a, *MNRAS*, 429, 2617  
 Ogrea, G. A., Brüggén, M., van Weeren, R. J., et al. 2013b, *MNRAS*, 433, 812  
 Okabe, N., Akamatsu, H., Kakuwa, J., et al. 2015, *PASJ*, 67, 114  
 Planck Collaboration, Ade, P. A. R., Aghanim, N., et al. 2011, *A&A*, 536, A8  
 Reichardt, C. L., Shaw, L., Zahn, O., et al. 2012, *ApJ*, 755, 70  
 Ricker, P. M. 2008, *ApJS*, 176, 293  
 Ricker, P. M. & Sarazin, C. L. 2001, *ApJ*, 561, 621  
 Sifón, C., Menanteau, F., Hasselfield, M., et al. 2013, *ApJ*, 772, 25  
 Springel, V., & Farrar, G. R. 2007, *MNRAS*, 380, 911  
 Stroe, A., Shimwell, T., Rumsey, C., et al. 2016, *MNRAS*, 455, 2402  
 van Weeren, R. J., Brunetti, G., Brüggén, M., et al. 2016, *ApJ*, 818, 204  
 van Weeren, R. J., Brüggén, M., Röttgering, H. J. A., & Hoeft, M. 2011, *MNRAS*, 418, 230  
 van Weeren, R. J., Röttgering, H. J. A., Brüggén, M., & Hoeft, M. 2010, *Science*, 330, 347  
 Zhang, C., Yu, Q., & Lu, Y. 2015, *ApJ*, 813, 129